Carbohydrate Polymers 368 (2025) 124178

Contents lists available at ScienceDirect

Carbohydrate Polymers

journal homepage: www.elsevier.com/locate/carbpol

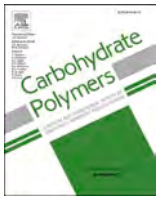

Electrically conductive and anti-inflammatory nerve conduits based on chitosan/hydroxyethyl cellulose hydrogel for enhanced peripheral nerve regeneration

Jiahui Song [a,1], Chenlong Liao [b,1], Zhengchao Yuan [a,1], Xiao Yu [a], Jie Cui [a], Yangfan Ding [a], Panpan Shang [c], Jinglei Wu [a], Binbin Sun [a], Mohamed EL-Newehy [d], Meera Moydeen Abdulhameed [d], Wenchuan Zhang [b,*], Gen Wen [e,*], Shichao Jiang [f,*], Xiumei Mo [a,c,**]

[a] State Key Laboratory for Modification of Chemical Fibers and Polymer Materials, Shanghai Engineering Research Center of Nano-Biomaterials and Regenerative Medicine, College of Biological Science and Medical Engineering, Donghua University, Shanghai 201620, China
[b] Department of Neurosurgery, Shanghai Ninth People's Hospital, Shanghai Jiao Tong University School of Medicine, Shanghai 200240, China
[c] Institute of Biomaterials and Biomedicine, School of Food and Pharmacy, Shanghai Zhongqiao Vocational and Technical University, Shanghai 201514, China
[d] Department of Chemistry, College of Science, King Saud University, P.O. Box 2455, Riyadh 11451, Saudi Arabia
[e] Department of Orthopedic Surgery, Shanghai Sixth People's Hospital Affiliated to Shanghai Jiao Tong University School of Medicine, National Center for Orthopaedic Medicine, Shanghai 200233, China
[f] Department of Orthopedics, Shandong Provincial Hospital Affiliated to Shandong First Medical University, Jinan 250021, China

ARTICLE INFO

Keywords:
Electrospinning
Conductive hydrogel
Anti-inflammatory drug
Nerve regeneration

ABSTRACT

Nerve guiding catheters (NGCs) are crucial for peripheral nerve repair, providing physical guidance and establishing a conducive microenvironment to nerve regeneration. In this study, we developed a bifunctional CS-HEC@PEDOT/SIM (CHPS) hydrogel-filled electrospun poly(L-lactide-co-caprolactone) (PLCL) conduit. The hydrogel matrix was fabricated using chitosan (CS) and hydroxyethyl cellulose (HEC) as the base materials, which exhibited excellent biocompatibility and degradability. Conductive poly(3,4-ethylenedioxythiophene) (PEDOT) was synthesized in situ within the matrix to establish stable electrostatic interactions with HEC, enhancing the electrical conductivity of the system. Additionally, the anti-inflammatory simvastatin (SIM) was uniformly dispersed throughout the hydrogel network through an optimized activation procedure. In vitro, the CHPS hydrogel exhibited promising electrical conductivity and sustained anti-inflammatory drug release. Furthermore, they supported neural cell proliferation and M2 macrophage polarization. In vivo, the CHPS hydrogel-filled conduits may create a favorable environment for electrical conductivity and inflammatory regulation, potentially promoting sciatic nerve regeneration in rats and facilitating partial recovery of motor function and nerve conduction. In conclusion, this approach may offer substantial potential for advancing nerve repair strategies and inspiring future clinical applications in the treatment of peripheral nerve injuries.

1. Introduction

Peripheral nerve injury (PNI) is a common clinical condition, typically caused by trauma or iatrogenic injury, resulting in severe sensory and motor dysfunction in patients (Osborne et al., 2018). Although peripheral nerves possess some regenerative capacity, this intrinsic self-repair ability is notably limited, with only approximately 25 % of patients achieving full motor function recovery (Mahar & Cavalli, 2018). Autologous transplantation is considered the gold standard in clinical practice for repairing nerve defects. However, this technique has several notable limitations, including donor site morbidity, size mismatch, and unsatisfactory functional recovery (Singh et al., 2022; Zuo & Borschel,

* Corresponding authors.
** Correspondence to: X. Mo, State Key Laboratory for Modification of Chemical Fibers and Polymer Materials, Shanghai Engineering Research Center of Nano-Biomaterials and Regenerative Medicine, College of Biological Science and Medical Engineering, Donghua University, Shanghai 201620, China.
E-mail addresses: Zhangwench88@sjtu.edu.cn (W. Zhang), wengen@sjtu.edu.cn (G. Wen), mailjsc@163.com (S. Jiang), xmm@dhu.edu.cn (X. Mo).
[1] Jiahui Song, Chenlong Liao, and Zhengchao Yuan are co-first authors.

https://doi.org/10.1016/j.carbpol.2025.124178
Received 1 May 2025; Received in revised form 27 July 2025; Accepted 3 August 2025
Available online 7 August 2025

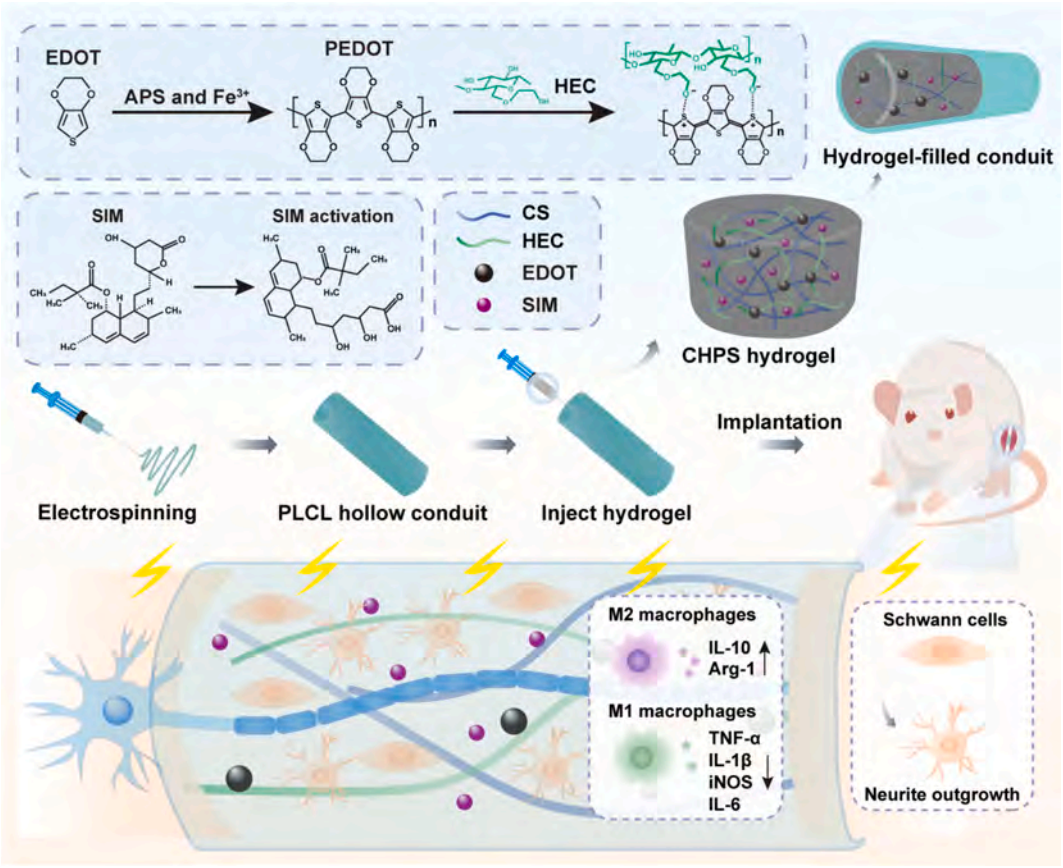

Scheme 1. Schematic illustration of the fabrication of conductive and anti-inflammatory CHPS hydrogel-filled nerve guidance conduits using electrospinning.

2021). Nerve guidance conduits (NGCs) have emerged as an effective strategy for nerve defects due to their capability to direct axonal extension along the longitudinal axis of the conduit (Gong et al., 2022; Wu et al., 2023). The reconstruction process subsequent to PNI involves multiple interlaced and sequential phases, such as Wallerian degeneration, debris removal, Büngner band formation, axon regeneration, and functional remodeling (Liu & Duan, 2023). Consequently, a unifunctional nerve conduit is insufficient to meet the multifaceted biological demands of peripheral nerve regeneration across these different stages, underscoring the clinical necessity of developing advanced NGCs to enhance the overall efficacy of peripheral nerve repair (Deng et al., 2022; Li et al., 2024).

The peripheral nerve is exposed to a complex electrophysiological environment, where the bioelectric field supports the conduction of neural signals and maintains the normal physiological function of peripheral nerves (Han et al., 2024; Liu et al., 2021). Conductive materials combined with exogenous electrical stimulation (ES) have been demonstrated to confer electrical conductivity to NGCs, thereby activating relevant signaling pathways within the cells, promoting axonal extension, and facilitating nerve regeneration (Gu et al., 2022; Yu et al., 2025; Zhang et al., 2023). Recently, biocompatible electroconductive hydrogels mimicking the mechanical and electrical properties of native nerve tissue have been developed to promote neuronal differentiation and axonal regrowth by providing a supportive three-dimensional biomimetic microenvironment (Fan et al., 2025; Jin et al., 2025; Liang et al., 2023). Accordingly, the integration of electroconductive components into a hydrophilic matrix can simultaneously provide biomimetic softness conducive to nerve regeneration and improve intercellular electrical signal transmission (Fan et al., 2022). Poly(3,4-ethylenedioxythiophene) (PEDOT), a conductive polymer that has been extensively studied, has been shown to support neuronal cell proliferation and synaptic extension, demonstrating its potential for applications in nerve injury treatment (Escobar et al., 2023). However, several drawbacks of PEDOT restrict its practical application, such as poor solubility, complicated processing, and inferior degradation properties (Spencer et al., 2018). The negative charge of the hydroxyl group in biodegradable hydroxyethyl cellulose (HEC) and the positive charge in PEDOT combine to form electrostatic interactions, which can improve the conductivity of materials (Park et al., 2022). In addition to improving the properties of PEDOT, HEC has also been combined with chitosan (CS) to overcome the limitations of CS-based scaffolds, such as weak mechanical strength and rapid degradation (Hoemann et al., 2007; Wang et al., 2017). CS is a naturally abundant polysaccharide with excellent biocompatibility, biodegradability, and antioxidant properties, making it widely used in neural tissue engineering (Wang et al., 2019). The hydroxyl groups of HEC and the amino groups of CS can be physically cross-link by hydrogen bonding, leading to the spontaneous formation of hydrogels without external triggers and making the gelation process fast and simple (Yan et al., 2010). This combination of CS, HEC, and PEDOT was first utilized to develop conductive hydrogels.

Despite the promising outcomes of conductive hydrogels in peripheral nerve repair, including improved neural signal conduction and accelerated tissue regeneration, the potential to induce a foreign body immune response upon implantation remains a significant concern, which may exacerbate local inflammation and compromise the efficacy of nerve repair. Consequently, modulating the immune microenvironment is critical for the application of NGCs. Hydrogels loaded with anti-inflammatory drugs allow for controlled drug release, enhancing treatment efficacy (Ye et al., 2024; Yu et al., 2024). Statins play a therapeutic role after PNI due to their anti-inflammatory, antioxidant, and immunomodulatory properties (Stüve et al., 2003). Moreover, studies have demonstrated that simvastatin (SIM) upregulates the expression of neurotrophic factors such as brain-derived neurotrophic factor (BDNF) and nerve growth factor (NGF) and facilitates peripheral nerve

regeneration in rats (Guo et al., 2017). However, directly incorporating SIM into hydrogels results in drug precipitation and a pronounced initial burst release (Yan et al., 2018). Therefore, prior to loading SIM into hydrogels, it is necessary to activate the drug to enhance its solubility and dispersibility within the hydrogel matrix.

This study developed a hydrogel matrix consisting of CS and HEC through physical cross-linking. Meanwhile, PEDOT was conjugated with HEC by electrostatic interactions. Following the activation of SIM, it was dissolved and uniformly dispersed within the hydrogel matrix. The prepared hydrogel was subsequently filled into electrospun poly(L-lactide-co-caprolactone) (PLCL) hollow tubes to obtain CS-HEC@PEDOT/SIM (CHPS) hydrogel-filled conduits (Scheme 1). We hypothesized that the CHPS hydrogel-filled conduit can create a conductive and anti-inflammatory microenvironment, which contributes to enhanced peripheral nerve regeneration. To verify this, physical properties of the CHPS hydrogels were characterized to assess their feasibility for peripheral nerve treatment. Biocompatibility and cell proliferative activity of hydrogels were evaluated using Schwann cells (SCs) and PC12 cells, while anti-inflammatory effects were analyzed in macrophages. Furthermore, the CHPS hydrogel-filled NGCs were implanted into rat sciatic nerve defect models. Comprehensive in vivo methods were conducted to evaluate nerve regeneration and the recovery of motor and sensory functions.

2. Materials and methods

2.1. Materials

Poly(L-lactide-*co*-caprolactone) (PLCL, LA:CL = 50:50, IV (dl/g): 1.76, Mn = 80 kDa) was provided by Jinan Daigang Co., Ltd. (Jinan, China). 1,1,1,3,3,3-hexafluoro-2-propanol (HFIP, 920-66-1) was purchased from Shanghai Darui Fine Chemical Co., Ltd. (Shanghai, China). Chitosan (CS, 9012-76-4, Mw = 70 kDa, deacetylation degree ≥ 95 %) was provided by Macklin (Shanghai, China). Hydroxyethyl cellulose (HEC, 9004-62-0, Mw = 250 kDa, molar degree of substitution = 1.0–1.2) was from Meryer (Shanghai, China). Simvastatin (SIM, 79902-63-9) was from Macklin (Shanghai, China). 3,4-ethylenedioxythiophene (EDOT, 126213-50-1) and ferric nitrate (7782-61-8) were purchased from Adamas-beta (Basel, Switzerland). Ammonium persulfate (APS, 7727-54-0) was bought from China National Pharmaceutical Group (Shanghai, China). Schwann 96 cells (SCs) and PC12 cells were provided by the Institute of Biochemistry and Cell Biology (Shanghai, China).

2.2. Fabrication of PLCL NGCs

PLCL (0.8 g) was dissolved in HFIP (10 mL) and stirred for 12 h until fully dissolved to prepare the spinning solution. For electrospinning (Yongkang Leye Technology Development Co., Ltd. SS-3556H, Beijing, China), the solution was dispensed through a syringe at a flow rate of 1 mL/h. A voltage of 12 kV was applied to the 20 G needle. Nanofibers were collected on a rotating collector at 200 rpm to produce conduits.

2.3. Fabrication of hydrogels

CS (0.4 g) was suspended in deionized water (10 mL) containing acetic acid (100 μL) and stirred overnight. HEC (0.3 g) was dissolved in deionized water (10 mL) and stirred overnight. The CS and HEC solutions were mixed 1:1 to obtain CH hydrogels. For the preparation of CHP hydrogels, HEC (0.3 g), EDOT (0.02 g), ammonium persulfate (0.01 g), and ferric nitrate (0.002 g) were added to deionized water (10 mL) and stirred overnight. This solution was then mixed with the CS solution at a ratio of 1:1 to obtain the CHP hydrogels. In the preparation of CHPS hydrogels, the SIM (0.5 mg/mL) needed to be activated first. In detail, SIM was dissolved in a solvent mixture consisting of distilled water (75 %), absolute ethanol (10 %), and 0.1 M NaOH (15 %). The solution was then incubated at 50 °C for 2 h and the pH was adjusted to 7.2 (Montaner et al., 2016). Subsequently, HEC (0.3 g), EDOT (0.02 g), ammonium persulfate (0.01 g), and ferric nitrate (0.002 g) were added into this solution (10 mL) and stirred overnight. Then, this solution and CS solution were mixed at a ratio of 1:1 to obtain CHPS hydrogels.

2.4. Fabrication of hydrogel-filled nerve conduits

To fabricate the hydrogel-filled nerve guidance conduits, the prepared CH, CHP, and CHPS hydrogels were carefully injected into PLCL conduits using a syringe. The hydrogel volume was adjusted to ensure complete filling of the lumen.

2.5. Characterization of hydrogels

2.5.1. Scanning electron microscopy (SEM)

The morphological characteristics of hydrogels were observed by a Scanning Electron Microscope (SEM, Hitachi TM-1000, Japan). The samples were frozen at −80 °C for 12 h and subsequently lyophilized for 3 days to preserve their original structure. Then the hydrogel samples were cut into small pieces (5 mm × 5 mm) and sputter-coated with Au for 60 s for further scanning examination.

2.5.2. Electrical properties

The resistance of hydrogels was determined by the four-probe method (ST25588-F01, China). The hydrogel samples were cut into rectangular shapes with dimensions of 20 mm × 10 mm × 2 mm (length × width × thickness), and the cross-sectional area (A) was determined by measuring the width and thickness with vernier calipers. The conductivity (σ) was calculated from the equation:

$$\sigma = \frac{L}{AR}$$

R represented the resistance of hydrogels in "MΩ"; L was the distance between the two electrodes in "cm"; and A was the cross-sectional area of hydrogels in "cm^2".

Electrochemical impedance spectroscopy (EIS) was carried out on an electrochemical workstation with a three-electrode system. Rectangular hydrogel samples with dimensions of 10 mm × 10 mm × 2 mm (length × width × thickness) were prepared for testing. In brief, 0.1 M phosphate buffered saline (PBS) was used as the electrolyte. The hydrogel sample was placed at the working electrode, while a saturated calomel electrode (SCE) and a platinum (Pt) wire served as the reference and counter electrodes, respectively. EIS was then performed with a frequency range from 10^{-2} to 10^{6} Hz.

All electrical measurements were performed at room temperature (25 ± 1 °C) and a relative humidity of 55 ± 5 % to ensure consistent environmental conditions.

2.5.3. Mechanical properties of hydrogels

The mechanical properties of the hydrogels were tested using a universal testing machine (HY-940FS, China) at room temperature (25 ± 1 °C) and a relative humidity of 55 ± 5 %. The hydrogels were molded into cylinders with a diameter of 12 mm and a height of 10 mm. Mechanical compression experiments were performed on the cylindrical samples at a rate of 5 mm/min, resulting in a strain rate of 0.0083 s^{-1}. A 20 N mechanical sensor was used to record the stress-strain result.

2.5.4. Porosity and water absorption rate

The porosity of hydrogels was measured using the ethanol substitution method. It was determined based on the amount of ethanol absorbed by dry hydrogels (5 mm in thickness and 8 mm in diameter), according to the following equation:

$$\text{Porosity}\ (\%) = \frac{W_2 - W_1}{D \times V} \times 100\%$$

where W_1 is the weight of dry hydrogel, and W_2 is the weight of wet

hydrogel, D is the ethanol density at room temperature, V is the volume of the wet hydrogel. The V was calculated by the actual thickness and diameter of the samples. Test 6 times, calculate the means.

To evaluate the water absorption of the hydrogel, the dry weight of the sample (Wd) was measured, and then the sample was immersed in the PBS solution at room temperature (25 ± 1 °C). After removing the sample, excess water was blotted off from the surface using filter paper. The wet weight of the sample (Ws) was then reweighed. The swelling ratio was calculated as follows:

$$\text{Water absorption rate } (\%) = \frac{W_s - W_d}{W_d} \times 100\%$$

2.5.5. The release of SIM in CHPS hydrogels

The CHPS hydrogel was immersed in 10 mL of PBS in a 37 °C incubator. At each predetermined time point, 3 mL of PBS in the release system was replaced with 3 mL of fresh PBS solution. The concentration of released SIM was measured at a wavelength of 238 nm using an ultraviolet-visible (UV–vis) spectrometer (KENREAL, USA).

2.5.6. In vitro antioxidant activity test

The antioxidant activity of hydrogels was determined by 2,2-Diphenyl-1-picrylhydrazyl (DPPH, 1898–66–4, MedChemExpress, New Jersey, USA). Briefly, 3 mL of DPPH ethanol solution (0.1 mmol/L) was combined with hydrogels (10 mg), and the mixture was then incubated for each predetermined time in the dark. After centrifugation, the absorbance of the solution was assessed at 517 nm using a microplate reader (Thermo Fisher Multiskan FC, USA). The scavenging rate of DPPH free radicals was calculated as follows:

$$\textit{DPPH scavenging rate } (\%) = \frac{D_0 - D_s}{D_0} \times 100\%$$

D_0 represented the absorbance of the DPPH working solution; D_s was the supernatant obtained after the assay.

2.5.7. In vitro degradation of PLCL conduits and hydrogels

The PLCL conduits and freeze-dried hydrogels were randomly divided into different experimental groups, with 3 samples in each group. The initial weight of each sample was recorded as W_0. The conduits and hydrogels were then submerged in PBS in a 37 °C incubator. At predetermined time points, the samples were removed from PBS, rinsed with distilled water, freeze-dried, and their final weights (W_1) were recorded. The residual mass of materials was calculated according to the formula:

$$\text{Residual mass } (\%) = W_1/W_0 \times 100\%$$

2.6. In vitro studies

2.6.1. Cell Culture

SCs and RAW 264.7 cells were cultured in DMEM containing 10 % fetal bovine serum (FBS) and 1 % penicillin/streptomycin (PS). PC12 cells were cultured in Roswell Park Memorial Institute (RPMI)-1640 medium supplemented with 20 % horse serum, 10 % FBS and 1 % PS. All reagents used for cell culture were purchased from Gibco.

2.6.2. Cell biocompatibility and proliferation assessment

The proliferation of SCs and PC12 cells was assessed using the Cell Counting Kit-8 (CCK-8, Beyotime, China) assay. SCs and PC12 cells at a density of 1×10^4 were seeded on CH, CHP, and CHPS hydrogels separately and cultured in a 37 °C incubator with 5 % CO_2 for 5 days. At 1, 3, and 5 days, cells were incubated for 1 h with 100 μL mL^{-1} CCK-8 solution. Besides, cells in the ES groups were subjected to ES with a potential of 100 mV for 1 h each day through a direct current power supply (HSPY-36-03, China). Additionally, cells were cultivated on hydrogels without ES as the control. Subsequently, 100 μL supernatant was added to a 96-well plate, and the optical density (OD) was measured at 450 nm using an enzyme labeling instrument (BioTech, Germany).

2.6.3. Immunofluorescence staining

Hydrogels were sterilized under ultraviolet light and then used to obtain extraction solutions. The hydrogels were immersed in different culture media for cell cultivation and then placed in a 37 °C incubator with 5 % CO_2. Cell seeding was performed as described previously. SCs and PC12 cells were fixed with 4 % paraformaldehyde and incubated in 0.1 % Triton X-100 for 5 min. Then, the cells were incubated in 1 % BSA-PBS for 30 min and washed thrice in PBS. Subsequently, SCs and PC12 cells were separately incubated with the primary antibody of rabbit anti-S100 antibody (1:200, Solarbio) or rabbit anti-200kD neurofilament antibody (NF200, 1:100, Solarbio) overnight at 4 °C. After rinsing with PBS 3 times, secondary antibodies, FITC-labeled goat antirabbit IgG H&L (1:200, Solarbio) or Cyc3-labeled goat antirabbit IgG H&L (1:200, Solarbio), were employed to stain the cells for 2 h at room temperature. Subsequently, cells were incubated with DAPI (1:500, Life Technologies, USA) for 10 min. Eventually, the stained samples were observed under a laser scanning confocal microscope (LSCM780NLO, Carl Zeiss, Germany).

2.6.4. Anti-oxidative properties

The anti-oxidative property of hydrogels was assessed by a reactive oxygen species (ROS) assay kit. RAW264.7 cells were seeded in 48-well plates at a density of 2×10^4 per well and cultured in a 37 °C incubator with 5 % CO_2 for 24 h. Then cells were induced with 100 ng mL^{-1} lipopolysaccharide (LPS) for 24 h. The extraction solution of hydrogels was used to culture cells. DCFH-DA was diluted to a final concentration of 10 μmol L^{-1} in serum-free medium. Each well was incubated with 200 μL of the solution and incubated for 20 min in the dark. Subsequently, the cells were incubated with DAPI for 10 min. The fluorescence staining of RAW264.7 cells was observed using a fluorescence microscope.

2.6.5. Immunomodulatory properties

Flow cytometry was employed to evaluate the phenotype polarization of RAW264.7 cells to further assess the anti-inflammatory properties of hydrogels. The cells were inoculated in six-well plates at a density of 2×10^5 per well and cultured in a 37 °C incubator with 5 % CO_2. The culture medium was removed after 24 h. Following 12 h of stimulation with LPS (100 ng mL^{-1}), cells were further cultured with hydrogel extraction solution. A total of 2 μL CD86 and 2 μL CD206 working solutions were added to the cell suspension and transferred to flow cytometry tubes. RAW264.7 cells were incubated in the dark on ice for 30 min and finally analyzed by flow cytometry. The negative control without LPS (−LPS) and positive control with LPS (+LPS) were designated as control and LPS groups, respectively.

RAW264.7 cells were inoculated in 24-well plates and cultured in a 37 °C incubator with 5 % CO_2. After 24 h, the medium was replaced with fresh medium containing 100 ng mL^{-1} LPS for 12 h of stimulation. The cells were then cultured for an additional 5 days. Subsequently, RAW264.7 cells were fixed with 4 % paraformaldehyde and incubated in 0.1 % Triton X-100 for 5 min. Then the cells were incubated in 1 % BSA-PBS for 30 min and incubated with the primary antibody of rabbit anti-CD206 antibody (1:200, Solarbio) overnight at 4 °C. After washing, FITC-labeled goat anti-rabbit IgG H&L (1:200, Solarbio) was employed to stain the cells for 2 h at room temperature and then incubated with DAPI (1:200, Life Technologies, USA) for 10 min. Finally, the stained samples were observed under a laser scanning confocal microscope (LSCM780NLO, Carl Zeiss, Germany).

2.6.6. Gene expression

Total RNA was extracted from RAW264.7 cells using a total RNA extraction kit (Novoprotein, China) and reverse-transcribed into cDNA with a reverse transcription kit (Novoprotein, China). Real-time qPCR

(RT-qPCR) was carried out by the LightCycler 480 SYBR Green Master Mix (Takara, Japan). The experiment was repeated three times, and the results were analyzed by the $2^{-\Delta\Delta Ct}$ method. Table S1 lists the primers used in this study.

2.7. Animal experiments

2.7.1. Ethical statement

The animal experiments were sanctioned by the Animal Experimental Ethics Committee of Shandong provincial hospital affiliated to Shandong first medical university (No. 2024-78). All rats were housed in a highly sanitary and controlled environment with a 12-h light/dark cycle. The temperature was maintained at 22 °C, and the relative humidity was maintained at 55 %. Animals were provided with pathogen free food and water. They were housed in groups of three per cage to ensure social interaction and minimize stress. This study was conducted in accordance with the ARRIVE guidelines to ensure the rigorous and ethical reporting of animal experiments.

2.7.2. Subcutaneous implantation

Sprague-Dawley (SD) rats (male, aged 8 weeks, weighing 250 g) received subcutaneous implantation of CH (n = 3), CHP (n = 3), and CHPS NGCs (n = 3) at each time point, and analyses were conducted at 4 weeks and 8 weeks post-implantation. Rats were anesthetized with 40 mg kg^{-1} pentobarbital sodium intraperitoneally. After shaving the dorsal region of the rats, an incision was made to form a subcutaneous pocket. Conduits were subsequently implanted, and the incision was closed using 5–0 sutures. For postoperative pain management, buprenorphine (0.05 mg kg^{-1}) was administered subcutaneously immediately after surgery and every 12 h for 48 h. All animals were monitored daily for signs of distress or discomfort. After 4 and 8 weeks, the local fascial layers were dissected, and the NGCs were retrieved for further examination.

2.7.3. NGCs transplantation for peripheral nerve regeneration

A total of 48 SD rats (male, aged 8 weeks, weighing 250 g) were randomly assigned to 4 surgical groups: Autograft, CH, CHP, and CHPS. Within each group, 6 animals were designated for analysis at 6 weeks post-surgery and 6 at 12 weeks post-surgery. During the surgical procedure, the sciatic nerve in the right hind limb was exposed, and a 10 mm segment was resected to establish a sciatic nerve defect model under general anesthesia with pentobarbital sodium (40 mg kg^{-1}). In the autograft group, the resected nerves were reversed and sutured back to the nerve stumps. Besides, a 10 mm nerve guidance conduit was implanted between the distal and proximal nerve stumps, the conduits were implanted in the defect and nerve stumps were sutured with 8–0 sutures. Postoperative analgesia was provided using buprenorphine (0.05 mg kg^{-1}) every 12 h for 48 h to manage pain and reduce the likelihood of abnormal behaviors. In addition, all animals were closely monitored daily for signs of pain-related behaviors or self-injurious activities throughout the experimental period.

2.7.4. Functional evaluation

The functional recovery of the injured sciatic nerves was evaluated by walking track analysis, gastrocnemius wet weight measurement, and electrophysiological examination. One group of animals was evaluated at 6 weeks, and a separate group was evaluated at 12 weeks post-implantation. For walking track analysis, the surgically treated hind limb was stained red and the normal hind limb was stained blue after 6 and 12 weeks. The rats were then allowed to walk on the surface of a blank sheet of paper to record their footprints. Three rats in each experimental group were recorded and analyzed for three valid trials per rat at each time point. After the rat crawled, the white paper with footprints was collected for further analysis. The sciatic nerve function index (SFI) values, including print length (PL, distance from the third toe to the heel), toe spread (TS, length from the first to the fifth toe), and intermediate toe spread (IT, length from the second to the fourth toe), were calculated using the following formula:

$$SFI = -38.3 \times \frac{E \times PL - N \times PL}{N} \times PL + 109.5 \times \frac{E \times TS - N \times TS}{N} \times TS + 13.3 \times \frac{E \times IT - N \times IT}{N} \times IT - 8.8$$

where N and E indicate the normal and experimental sides, respectively. In this study, SFI values range from −100 to 0, with −100 representing total motor sciatic nerve dysfunction.

2.7.5. Electrophysiological analysis

After the rats were anesthetized, the damaged nerve and the ipsilateral gastrocnemius muscle were re-exposed. A bipolar stimulating electrode was placed on the sciatic nerve, and a needle recording electrode was inserted into the anterior tibialis muscle. Subsequently, a ground electrode was placed in the surrounding muscles. The amplitude of the evoked compound muscle action potentials (CMAPs) and nerve conduction velocity (NCV) were recorded by a portable biological-function experimental system (BL-420S, Tai Meng). A 10-mA current was used to constantly stimulate the rat for 1 ms. Although this intensity elicited stable responses across animals, no formal determination of maximal or supramaximal stimulation was performed.

2.7.6. Muscle weight ratio and histological assessment

The triceps surae muscle (TSM) of both hind limbs were weighed at 12 weeks to determine the muscle weight ratio (experimental side/normal side). For histological analysis, muscle tissues were fixed in 4 % paraformaldehyde for 24 h, embedded in paraffin, and cut into 5 μm thick cross-sections. Three sections per group were examined for cross-sectional morphology using Masson's trichrome staining. The diameter and the percentage of muscle fibers area were analyzed using ImageJ software.

2.7.7. Nerve histological assessment

For histological assessment, regenerated sciatic nerves in different NGCs were obtained using sutures as landmarks at 6 and 12 weeks post-surgery. Nerve samples were fixed in 4 % paraformaldehyde, embedded in paraffin, and sectioned into 5 μm thick transverse and longitudinal slices. These sections were stained with hematoxylin and eosin (H&E). Longitudinal sections of regenerated nerves after 12 weeks were fixed with 4 % paraformaldehyde for 24 h, embedded in paraffin, sectioned into 5 μm thick, and stained with Luxol fast blue (LFB). ImageJ software was used to measure the positive myelin area percentage from LFB staining. In addition, the gastrocnemius muscle from the operative leg was also collected and processed using the same fixation and embedding protocol, followed by Masson's trichrome staining. At least three sections per animal were selected for histological analysis.

2.7.8. Immunofluorescence analysis of regenerated nerve

For immunofluorescence staining, the longitudinal sections (5 μm thickness) were incubated with primary antibodies of rabbit anti-S100 (1:100, Solarbio) and rabbit anti-NF200 (1:100, Solarbio) overnight at 4 °C. To assess macrophage polarization within the regenerated nerves,

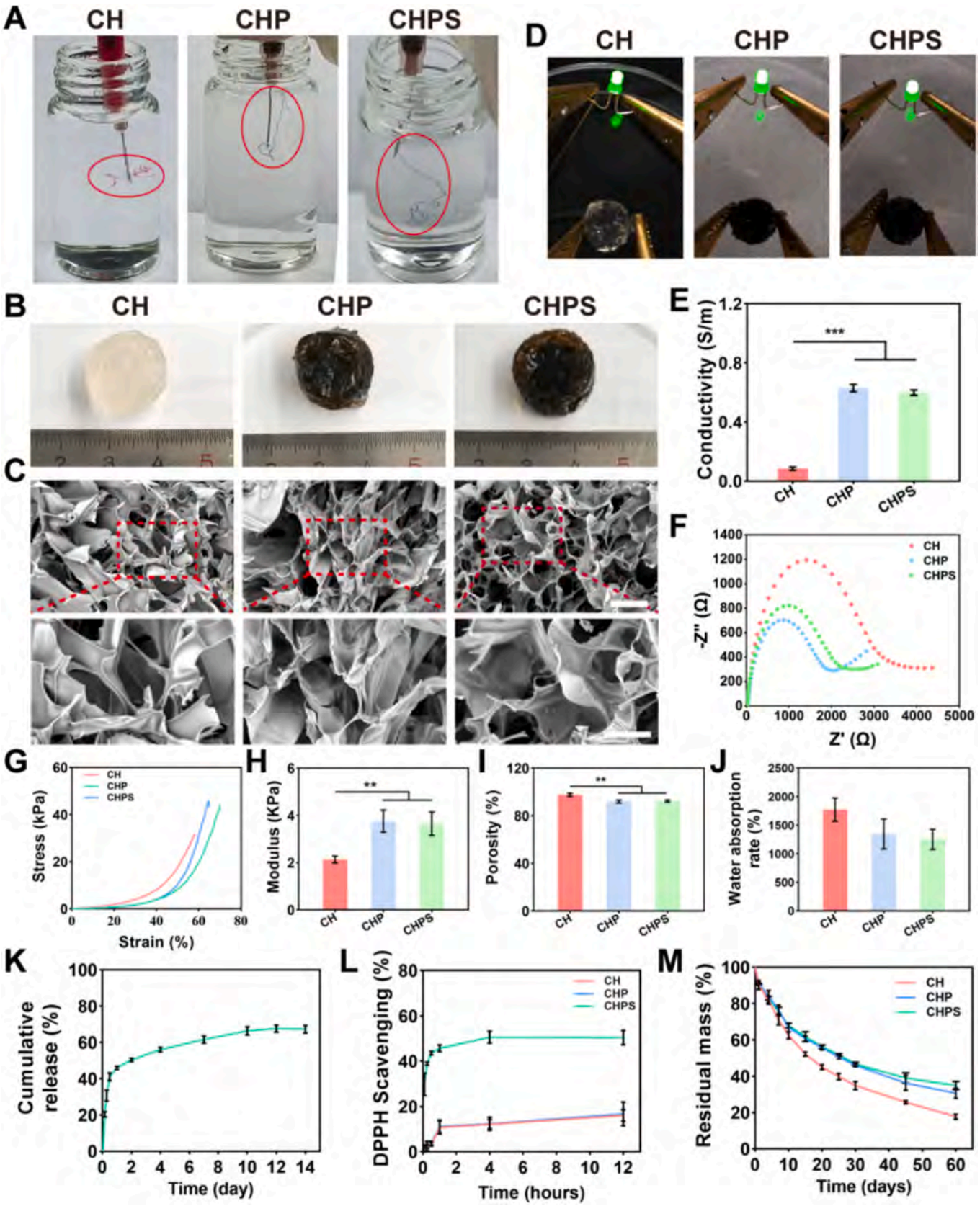

Fig. 1. Characterization of CH, CHP, and CHPS hydrogels. (A) The injectability of CH, CHP, and CHPS hydrogels. (B) Photographs of different groups of hydrogels. (C) SEM micrographs of hydrogels. Scale bar: 50 μm. (D) CH, CHP, and CHPS hydrogels utilized as electrically conductive paths for LED illumination. (E) Conductivity and (F) EIS image of CH, CHP, and CHPS hydrogels. (G) Mechanical compression curves and (H) compression modulus of these hydrogels. (I) Porosity and (J) water absorption rate of hydrogels. (K) Cumulative release profile of SIM in the CHPS hydrogel. (L) DPPH radicals scavenging ability and (M) in vitro degradation performance of hydrogels. $^{*}p < 0.05$, $^{**}p < 0.01$, $^{***}p < 0.001$.

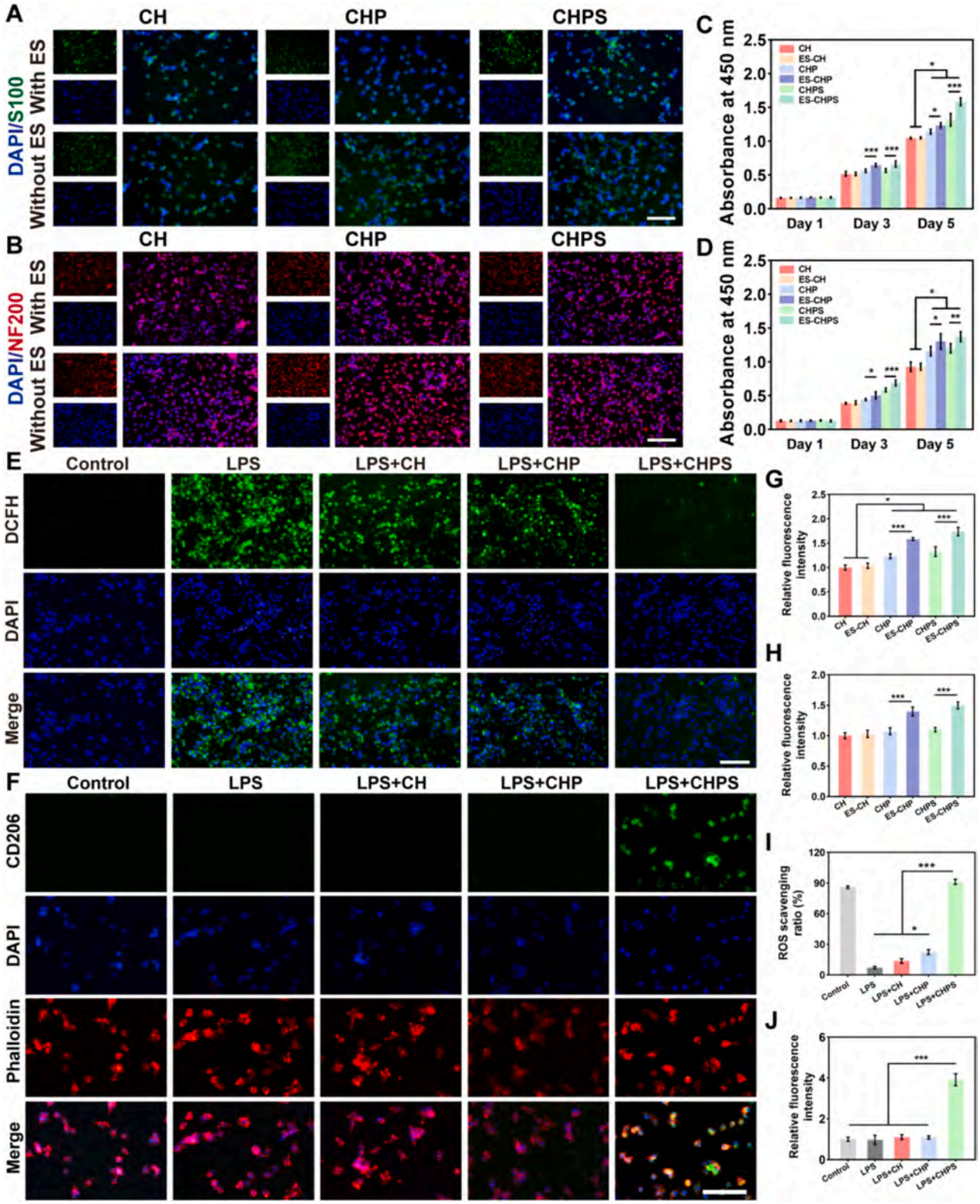

Fig. 2. Proliferation of neural cells and antioxidant properties of RAW 264.7 cells. (A) Immunofluorescence staining of S100 (green) and DAPI (blue) of SCs. Scale bar: 100 μm. (B) IF staining of NF200 (red) and DAPI (blue) of PC12 cells. Scale bar: 100 μm. Proliferation of (C) SCs and (D) PC12 cells in various hydrogels cultured with and without ES. (E) The antioxidant ability of LPS-induced RAW264.7 cultured in extraction solution, DCFH (green), DAPI (blue). Scale bar: 100 μm. (F) IF staining of CD206 (green), DAPI (blue), and Phalloidin (red) in LPS-induced RAW 264.7 cells cultured in extraction solution. Scale bar: 100 μm. Relative fluorescence intensity of (G) S100 in SCs and (H) NF200 in PC12 cells cultured with and without ES. (I) ROS scavenging ratio. (J) Relative fluorescence intensity of CD206. $^{*}p < 0.05$, $^{**}p < 0.01$, $^{***}p < 0.001$.

the sections were stained with polyclonal antibodies of rabbit anti-iNOS (M1, proinflammatory) (1:100, Solarbio), and rabbit anti-mannose receptor (CD206, M2, anti-inflammatory) (1:100, Solarbio). Next, the nerve sections were stained with FITC-labeled goat anti-rabbit IgG H&L (1:200, Solarbio) and Cy3-labeled goat anti-rabbit IgG H&L (1:200, Solarbio) and incubated for 1 h. Finally, the nerve sections were stained with DAPI (1:200, Solarbio) for 10 min. For quantitative analysis, three non-consecutive sections per animal were analyzed to quantify the positive area percentage of S100 and NF200, as well as the M2/M1 ratio, using ImageJ software.

2.8. Statistical analysis

All data were presented as mean ± standard deviation. Statistical analysis was performed using one-way ANOVA and Tukey's multiple comparison tests. $p < 0.05$, $p < 0.01$, and $p < 0.001$ were denoted as statistically significant differences by *, **, and ***, respectively.

3. Results and discussion

3.1. Characterizations of hydrogels

SEM micrographs of the PLCL membrane exhibited smooth and bead-free nanofibers, with an average diameter of 0.76 ± 0.12 μm (Fig. S1A and B). CH, CHP, and CHPS hydrogels exhibited rapid gelation within 5 min, and their injectability was shown in Fig. 1A. Digital photographs of hydrogels in Fig. 1B revealed that the CH hydrogel appeared colorless, while the CHP and CHPS hydrogels were black. To confirm the physical cross-linking of CS and HEC through hydrogen bonding in the hydrogel formation, FTIR spectroscopy was performed on CH hydrogels. The FTIR spectrum showed characteristic peaks of CS were observed at 3740 cm^{-1} attributed to NH stretching, CH stretching at 2860 cm^{-1}, C═O bonds at 1660 cm^{-1}, NH bending at 1590 cm^{-1}, and C—O stretching at 1070 cm^{-1} (Zhang et al., 2021). The main absorption peaks of HEC are -CH_2- and -OH at 2880 cm^{-1} and 3300 cm^{-1}, respectively, as well as the telescopic vibration peaks of HEC ring at 1120 cm^{-1} and 1030 cm^{-1} (Madivoli et al., 2023). The FTIR spectrum of CH showed the low-intensity absorption bands at 1660 cm^{-1}, corresponding to the C═O carbonyl stretching. This may be due to the formation of the hydrogen bonds between the carbonyl groups of CS and the hydroxyl groups of HEC (Fig. S2). The surface morphology of the materials was initially assessed using SEM, revealing a microporous structure characterized by interconnected internal pores (Fig. 1C). Enlarged local observation showed no obvious impurities attached to the inner walls of the CH and CHP hydrogel pores, indicating that EDOT was uniformly polymerized within the hydrogel without affecting its internal structure. However, precipitated particles were observed on the pore wall of the CHPS hydrogel, corresponding to phase separation between the hydrogel matrix and SIM, even though SIM had been activated (Yan et al., 2018). Besides, non-activated SIM was dispersed in water and stirred for 12 h to form a suspension. The SIM precipitated at the bottom of the bottle after standing, proving that SIM was a hydrophobic drug and insoluble in water (Fig. S3A and B). After forming a hydrogel, the hydrogel containing activated SIM was transparent. In contrast, the hydrogel containing non-activated SIM was milk-white, which further indicated that the non-activated SIM was difficult to dissolve in the hydrogel was poorly dispersed (Fig. S3C).

The inherent electroactivity of nerve tissues highlights the importance of improving the conductivity of artificial NGCs, as it contributes to the formation of a microenvironment conducive to nerve regeneration (Wang et al., 2024). All three types of hydrogels were capable of illuminating a light-emitting diode (LED) bulb, even the CH hydrogels that did not contain the conductive material PEDOT (Fig. 1D). This phenomenon can be attributed to the inherent water content within the hydrogels, which enables the formation of a closed electrical circuit. Specifically, the water in the hydrogels contains dissolved ions that can facilitate the movement of charge carriers, enabling sufficient conductivity to complete the circuit and power the LED. To further quantify the effect of PEDOT incorporation on the electrical conductivity of the hydrogels, the conductivity of CH, CHP, and CHPS hydrogels was tested. The results showed that the electrical conductivity of the CH, CHP, and CHPS hydrogels was 0.08 ± 0.01 S m^{-1}, 0.63 ± 0.02 S m^{-1}, and 0.59 ± 0.02 S m^{-1}, respectively. Notably, the electrical conductivity of CHP and CHPS hydrogels was significantly higher than that of CH hydrogels (Fig. 1E). The electrical conductivity of nerves has been reported to be approximately 0.39 S m^{-1}, and the CHP and CHPS hydrogels exhibited conductivity in the range of 0.1–1 S m^{-1}, matching or surpassing that of healthy nerve tissue (Lee et al., 2022). The diameter of the semicircle observed in the EIS plot reflected the charge transfer resistance, with a smaller diameter corresponding to lower impedance. The EIS results showed that the PEDOT-containing hydrogels (CHP and CHPS) exhibited significantly smaller semicircle diameters compared to the CH hydrogel, suggesting a notable reduction in impedance (Fig. 1F). The impedances of CHP and CHPS were similar, which was consistent with the results of the electrical conductivity. This enhancement in conductivity confirmed that the addition of PEDOT effectively improved the electrical conductivity of the hydrogels.

Nerve conduits need to provide adequate support and maintain a slight elasticity to cope with the friction and extrusion of the surrounding tissue, preventing conduit collapse or deformation during nerve regeneration (Wang et al., 2024). The mechanical tensile properties of the PLCL conduits are presented in Fig. S1C and D. The tensile strength of the conduits was 12.96 ± 1.03 MPa. It has been reported that human sciatic nerves can withstand a maximum stress of 1930 ± 50 kPa (Yu et al., 2013). The results indicated that the PLCL conduits met the necessary mechanical standards for nerve repair applications. In the mechanical compression experiment, all hydrogels showed good compressive properties with more than 50 % strain. The compressive modulus of the CHP and CHPS hydrogels containing PEDOT added was significantly higher than that of the CH group (Fig. 1G and H). These results suggested that adding PEDOT improved the mechanical properties of hydrogels, which was consistent with previous reports (Guan et al., 2022). The porosity and water absorption ratio of CHP and CHPS groups were lower than those of CH hydrogel, which may be due to the in situ polymerization of EDOT increasing the structural linkage of long molecular chain segments within the hydrogel (Fig. 1I and J). Although EDOT polymerized homogeneously, it partially clogged the micropores, reducing the pore size and decreasing the porosity of the hydrogel. Furthermore, the three groups of hydrogels exhibited high swelling rates, which ensured sufficient nutrients required for cell growth.

The intra-hydrogel SIM release was measured for 14 days. As depicted in Fig. 1K, the initial burst release of the SIM occurred within the first 24 h, accounting for approximately 45 % of the total release. This could be due to the rapid diffusion of a small fraction of SIM that was not fully integrated into the hydrogel matrix during fabrication. The drug release rate gradually decreased over time, with approximately 70 % of SIM released from the hydrogel, allowing its anti-inflammatory effect during the early stage of PNI (Shan et al., 2024). The antioxidant capacity of the hydrogel was evaluated using a DPPH radical scavenging assay (Fig. 1L). The free radical scavenging activity of the CHPS hydrogel reached 50 % after 12 h, primarily attributed to the excellent antioxidant properties of SIM (Jafari et al., 2021). In addition, the CH and CHP hydrogels exhibited 16 % free radical scavenging, probably due to the antioxidant properties exerted by the CS in the hydrogel (Wang et al., 2024). In vitro degradation studies showed rapid degradation of the CH hydrogel, with only 20 % remaining after 60 days (Fig. 1M). The degradation rates of CHP and CHPS were slower compared to the CH hydrogel, with 40 % mass remaining after 60 days, indicating that the in situ polymerization of PEDOT resulted in higher cross-linking densities in these hydrogels. In vitro degradation experiments proved that the three hydrogels had good degradation properties and were suitable for in vivo application. However, in vitro degradation

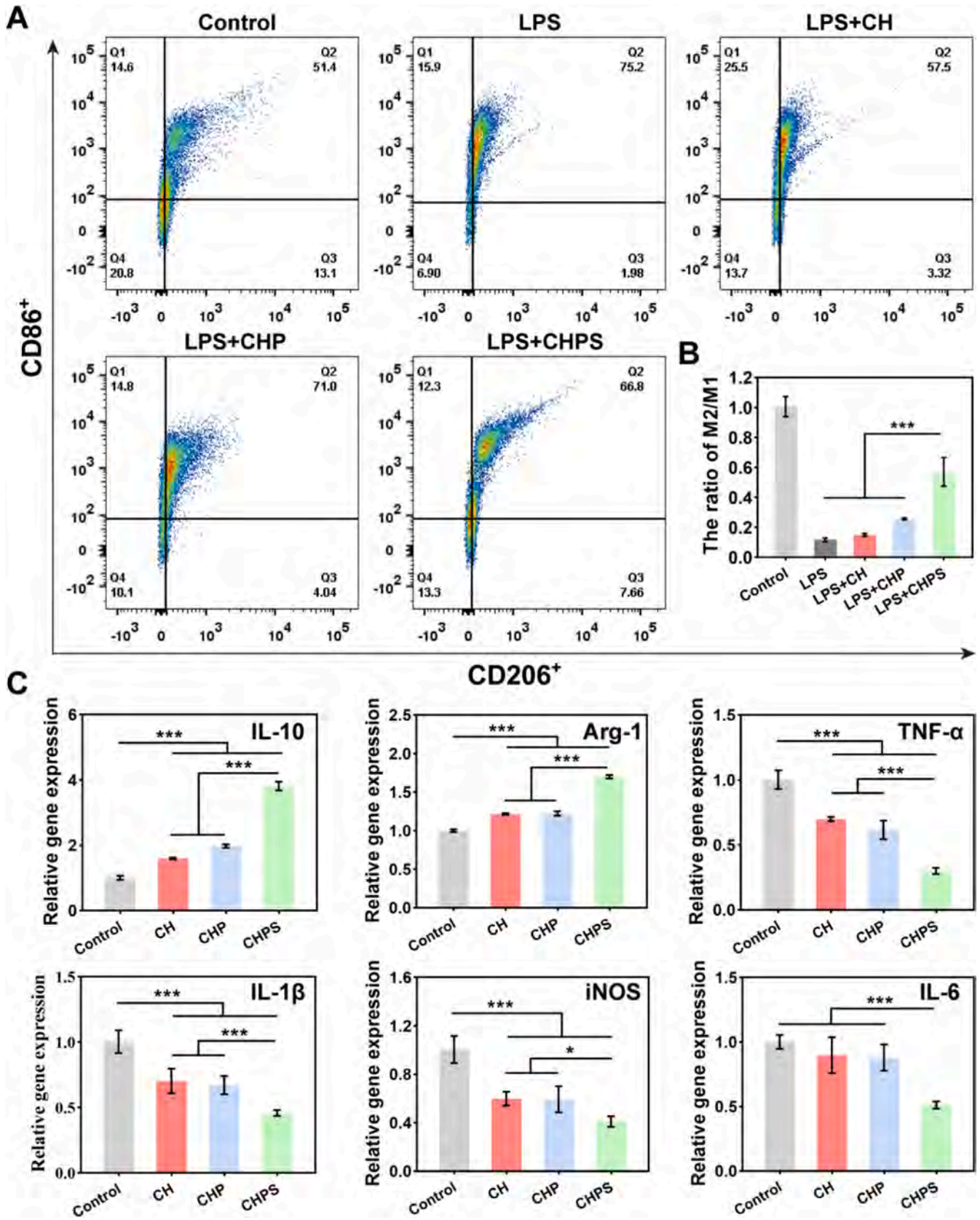

Fig. 3. The anti-inflammatory ability of conditioned medium obtained from CH, CHP, and CHPS hydrogels. (A) Flow cytometry analysis of $CD86^+$ and $CD206^+$ expression of RAW 264.7 macrophages cultured with the conditioned medium obtained from hydrogels. (B) The ratio of M2/M1 calculated by flow cytometry. (C) Quantitative analysis of IL-10, Arg-1, TNF-α, IL-1β, iNOS, and IL-6 gene expression in RAW 264.7 macrophages. *$p < 0.05$, **$p < 0.01$, ***$p < 0.001$.

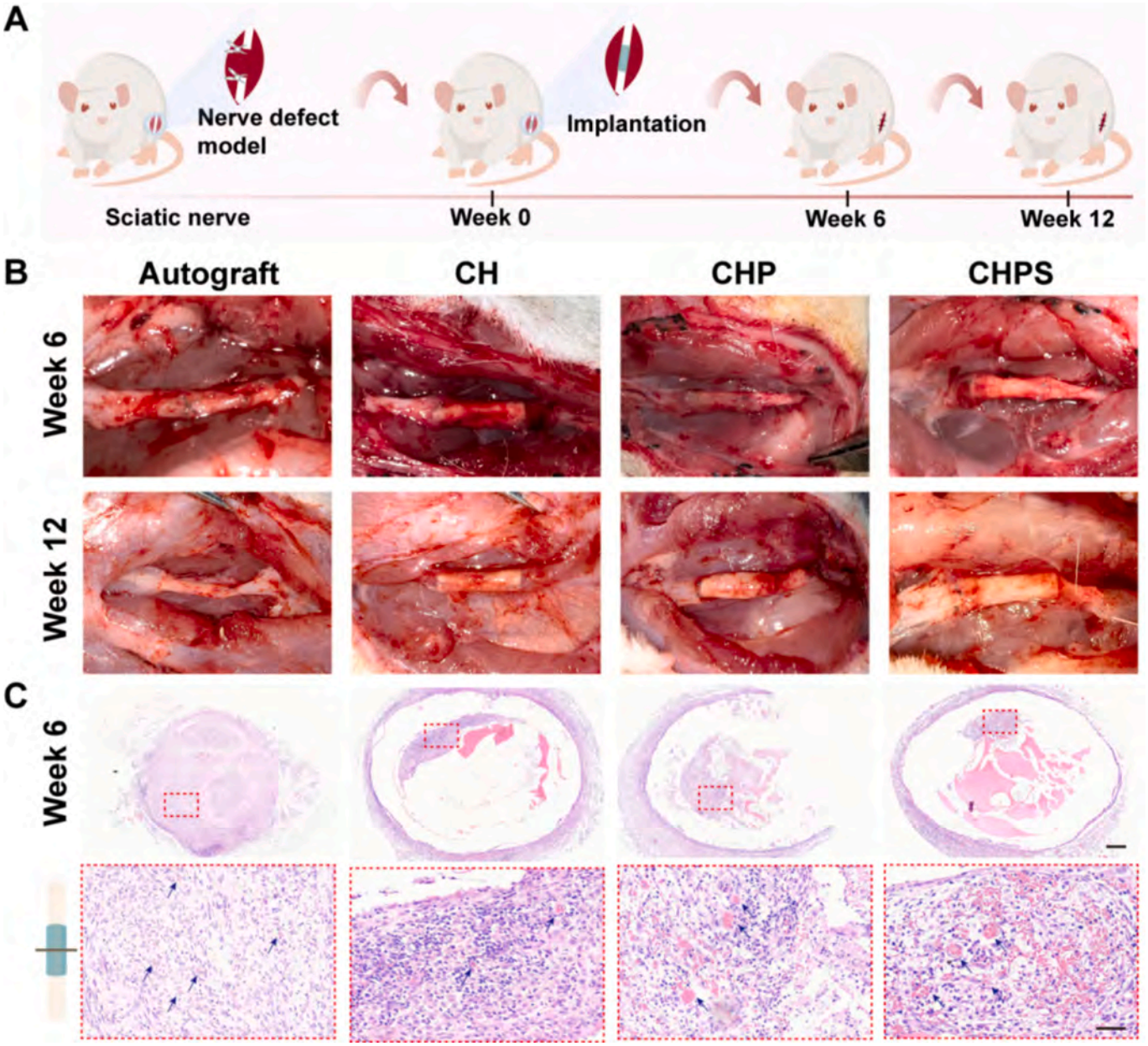

Fig. 4. Gross observation and H&E staining of the section from autologous transplantation, CH, CHP, and CHPS conduits. (A) Schematic illustration of NGCs transplantation. (B) Photographs of surgical implantation. (C) Cross sections of intermediate of autologous transplantation and conduits at 6 weeks stained with H&E. Scale bar: 200 μm. Scale bar: 50 μm. Blue arrows indicate neovascularization.

results of PLCL conduits indicated a slow degradation rate, with only 4 % degradation after 30 days (Fig. S1E). It will take a prolonged period for PLCL materials to achieve complete degradation (Abe et al., 2020).

3.1.1. Cultivation of SCs and PC12 cells with ES in vitro and anti-inflammatory

Cell proliferation and expression of specific fluorescent proteins were detected after seeding SCs and PC12 cells on the hydrogels. As shown in Fig. 2C, SCs exhibited higher proliferation on CH, CHP, and CHPS hydrogels, suggesting good biocompatibility of these materials. After 3 and 5 days of culture, SCs proliferated more rapidly on CHP and CHPS hydrogels under ES, indicating that the presence of PEDOT promoted the proliferation of SCs. The proliferation trend of PC12 cells was similar to that of SCs. Under ES, PC12 cells cultured on CHP and CHPS hydrogels showed significantly higher proliferation rates on days 3 and 5 compared to those cultured on hydrogels without ES (Fig. 2D).

Representative fluorescence images of SCs and PC12 cells cultured on the hydrogels after 5 days are presented in Fig. 2A and B, respectively. The relative fluorescence intensity of S100 protein expression in SCs is shown in Fig. 2G. Under ES, the fluorescence intensity of S100 in CHP and CHPS hydrogels was significantly enhanced and was higher than that in the CH group. The expression of NF200 protein was considerably increased in PEDOT-containing CHP and CHPS hydrogels under external ES. However, no significant difference in NF200 expression was observed between the CHP and CHPS groups without ES and the CH group (Fig. 2H). The presence of PEDOT in the hydrogel was shown to enhance the electrical conductivity of the material, which facilitated the transmission of electrical signals in electroactive tissues. When combined with appropriate ES, this conductive environment effectively promoted cell proliferation and supported cellular functions (Xu et al., 2023; Zhou et al., 2018). However, the detailed mechanisms by which conductive hydrogels combined with ES affect neural cells

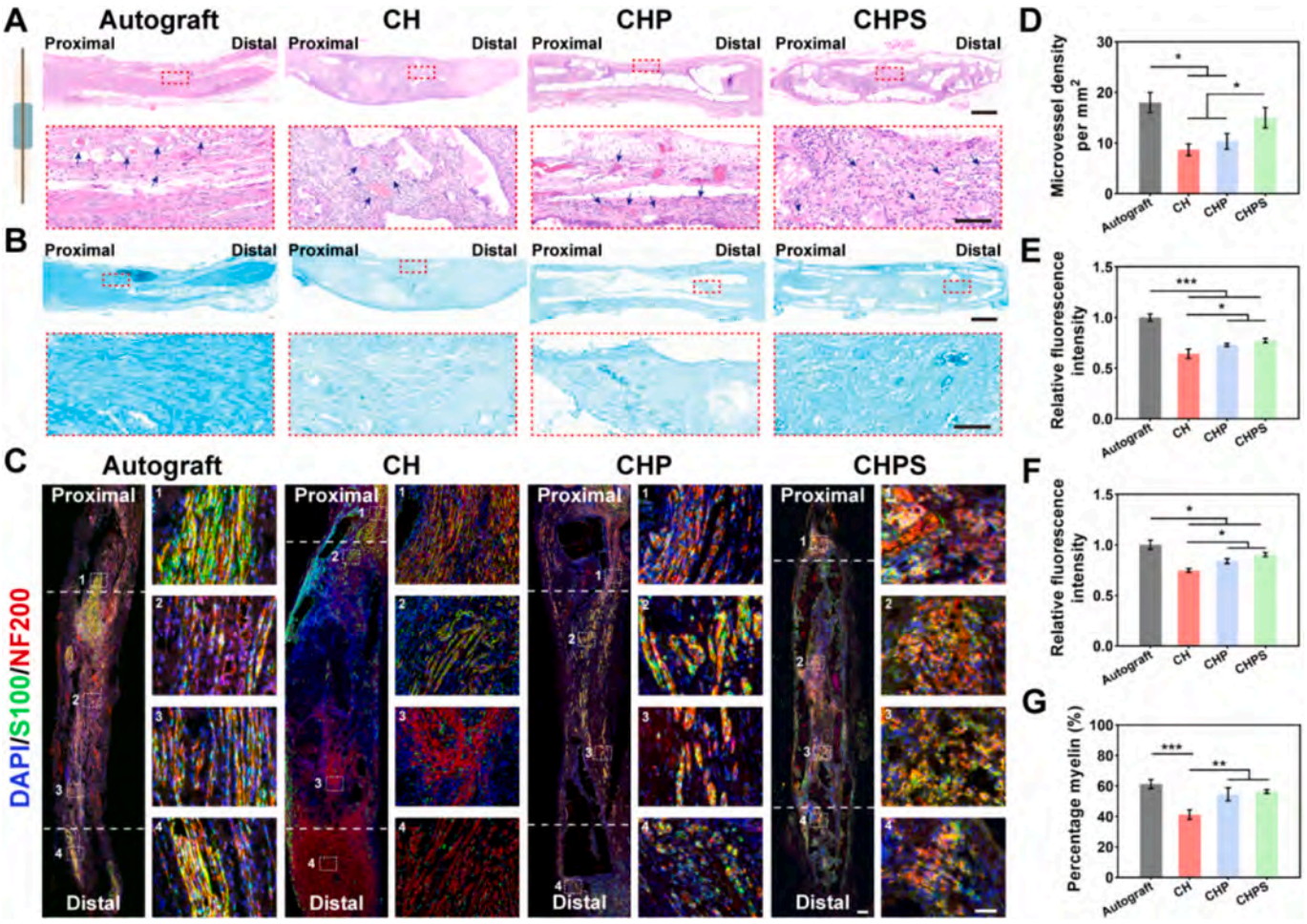

Fig. 5. Histological morphological evaluation of autologous transplantation, CH, CHP, and CHPS conduits at 12 weeks. (A) Longitudinal sections of autologous transplantation and conduits at 12 weeks stained by H&E. Scale bar: 1 mm. Scale bar: 100 μm. Blue arrows indicate neovascularization. (B) Longitudinal sections of autologous transplantation and conduits at 12 weeks stained by LFB. Scale bar: 1 mm. Scale bar: 100 μm. (C) Immunofluorescence staining images of longitudinal sections of S100 (green), NF200 (red), and nuclei (blue). Scale bar: 200 μm (low magnification) and 50 μm (high magnification). (D) Microvessel density calculated based on different groups. (E) Relative fluorescence intensity of S100. (F) Relative fluorescence intensity of NF200. (G) The positive area percentage of myelin calculated by LFB staining images. $^{*}p < 0.05$, $^{**}p < 0.01$, $^{***}p < 0.001$.

remain to be studied.

The intracellular ROS scavenging ratio was measured by LPS-induced DCFH-DA green fluorescence in RAW 264.7 cells (Fig. 2E and I). The CH, CHP, and CHPS hydrogels showed higher ROS scavenging ratios compared to the LPS group, which can be attributed to the antioxidant properties of CS within the hydrogels (Bashir et al., 2022). The incorporation of PEDOT significantly enhanced the ROS scavenging capacity of CHP hydrogels compared to CH hydrogels. This improvement was primarily attributed to the conjugated backbone of PEDOT, which facilitated electron donation for ROS neutralization and exhibited intrinsic antioxidant properties (Zhou et al., 2022). Moreover, CHPS hydrogels showed a significantly lower number of positive cells compared to other LPS-induced groups, indicating the effective antioxidative property of SIM. To examine the effect of hydrogels on macrophage polarization, CD206 staining, a marker for M2 macrophage polarization, was performed (Fig. 2F). Macrophages cultured on CHPS hydrogels expressed higher levels of CD206 than other groups (Fig. 2J).

To assess the anti-inflammatory response induced by the hydrogels, the expression levels of CD86 and CD206 were detected using flow cytometry (Fig. 3A). Quantitative results revealed that the CD206/CD86 ratio in the CHPS hydrogel was significantly higher than other groups except the control group, which demonstrated that the CHPS hydrogel promoted macrophage polarization toward the M2 phenotype due to the release of SIM (Fig. 3B). To evaluate the effects of hydrogels on RAW264.7 cells, mRNA expression levels of anti-inflammatory and pro-inflammatory cytokines were analyzed by qPCR. The CHPS group showed significantly upregulated expression of the anti-inflammatory markers IL-10 and Arg-1 compared to the CH and CHP groups. In contrast, the expression levels of pro-inflammatory cytokines, including TNF-α, IL-1β, iNOS, and IL-6, were significantly lower in the CHPS group relative to the other groups (Fig. 3C). The results of qPCR further confirmed that the CHPS hydrogels exhibited the anti-inflammatory property.

3.1.2. Morphological assessment of regenerated nerves

To evaluate the efficacy of nerve repair in a rat model of sciatic nerve defect, hydrogel-filled conduits were implanted and then harvested for comprehensive histological analysis at 6 and 12 weeks after surgery (Fig. 4A). At 6 weeks, both ends of the conduit had successfully fused with the epineurium. By the 12-week time point, none of the experimental groups displayed signs of neuroma formation (Fig. 4B). Intermediate cross-sections of the peripheral nerve grafts were examined at 6 weeks post-implantation, while longitudinal sections were prepared at 12 weeks to better evaluate nerve tissue regeneration. Both time points were subjected to H&E staining for histological analysis. At 6 weeks post-implantation, histological analysis revealed partial hydrogel degradation within all conduits (Fig. 4C). H&E staining of longitudinal sections at 12 weeks post-implantation revealed that while the conduits

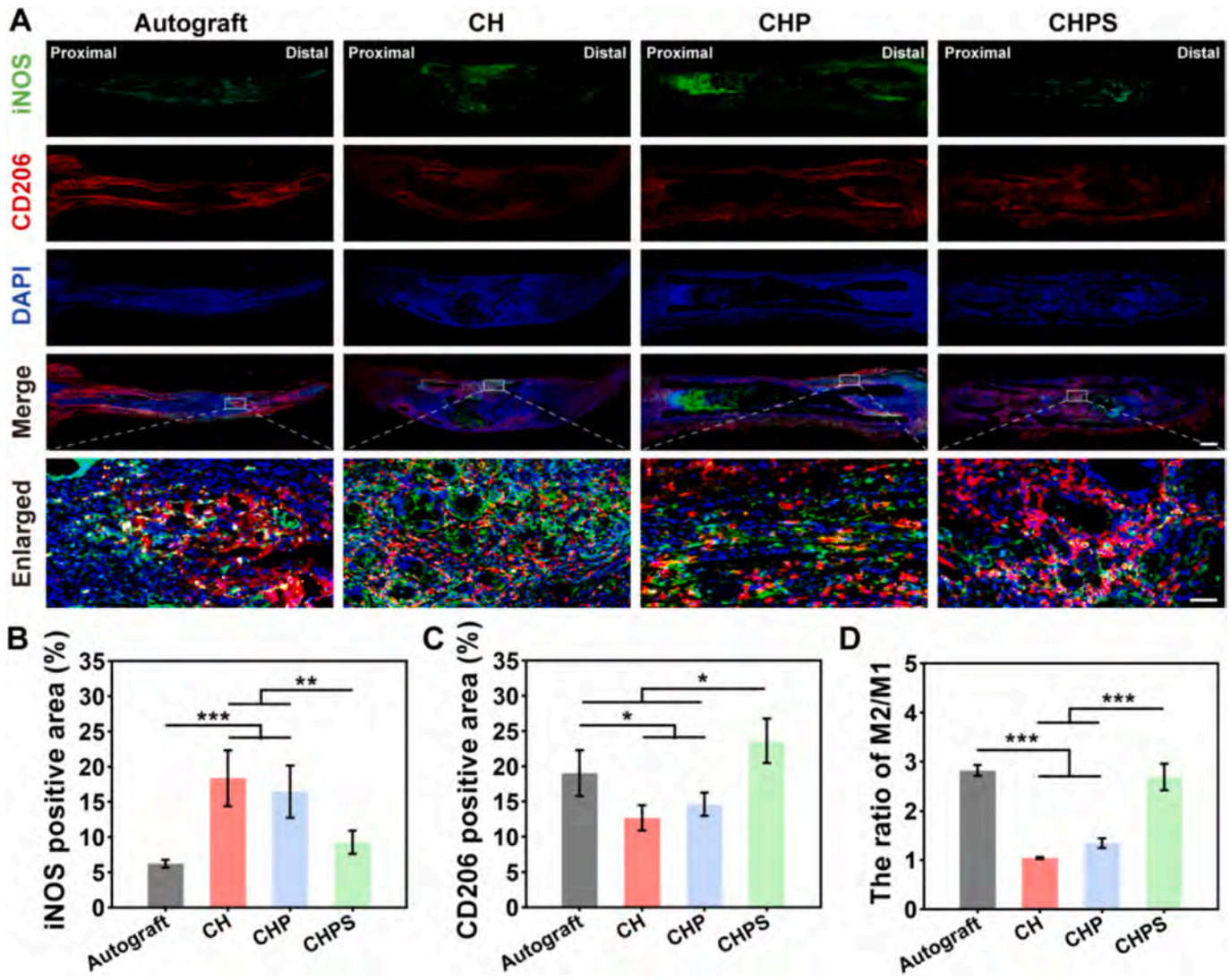

Fig. 6. Immunofluorescence staining of regenerated nerve tissues from different groups in iNOS and CD206 after 12 weeks. (A) Immunofluorescence staining of regenerated nerve tissues in iNOS (green) and CD206 (red). Scale bar: 500 μm. Scale bar: 50 μm. (B) Quantitative analysis of iNOS expression positive areas. (C) Quantitative analysis of CD206 expression positive areas. (D) Quantitative analysis of the ratio between M2/M1. *p < 0.05, **p < 0.01, ***p < 0.001.

partially maintained their structural integrity, the internal hydrogel was completely degraded with extensive neural regeneration extending along all conduits (Fig. 5A). Further results from subcutaneous implantation indicated a substantial amount of undegraded the hydrogel within conduits at 4 weeks. Significant degradation was observed by 8 weeks, confirming the gradual degradation of hydrogels (Fig. S4). The reduction in hydrogel volume and its gradual degradation created sufficient space for peripheral nerve extension within the conduit, effectively minimizing the risk of nerve compression.

3.1.3. Histological analysis of regenerated sciatic nerves

The continuous supply of oxygen and nutrients through vascularization plays a critical role in peripheral nerve regeneration (Saffari et al., 2020). Following implantation of conduits, vascularization initiates bidirectionally from the proximal and distal nerve stumps, gradually extending toward the central region of the conduit (Chalfoun et al., 2003). Although the progression of vascularization into the center of NGCs is time-dependent, regenerated microvessels were observed in the middle sections of all experimental groups at 6 weeks post-transplantation (Fig. 4C). At 12 weeks post-transplantation, the regenerated microvessels were macroscopically observed and marked with blue arrows in Fig. 5A. Further quantitative analysis of microvessel density showed that the CHPS group exhibited vessel density comparable to that of the autograft group, with both showing significantly higher values than the CH and CHP groups (Fig. 5D). Statistical analysis of microvessel diameters revealed consistent results (Fig. S5). The improved vascularization observed in the CHPS group can be attributed to the incorporation of SIM, a potent angiogenic agent recognized for its capacity to promote endothelial cell function, stimulate nitric oxide (NO) release, and facilitate the migration and proliferation of endothelial cells (Sharma et al., 2023; Yu et al., 2020). Additionally, LFB staining revealed that more nerve myelin was observed in the CHP, CHPS, and autograft groups compared to the CH group (Fig. 5B). To obtain an accurate assessment, the percentage of positive myelin area in the CHP and CHPS groups was comparable to that in the autograft group, and significantly higher than that in the CH group after 12 weeks (Fig. 5G). Immunofluorescence staining of longitudinal sections was employed to evaluate remyelination and axonal regeneration through the expression of S100 and NF200 proteins, respectively (Fig. 5C). Among the four experimental groups, distinct differences in staining intensity were observed. Further analysis revealed notably higher staining intensities of S100 and NF200 in the autograft, CHP, and CHPS groups than in the CH group (Fig. 5E and F). These results showed that CHP and CHPS hydrogel-filled nerve conduits effectively promoted peripheral nerve

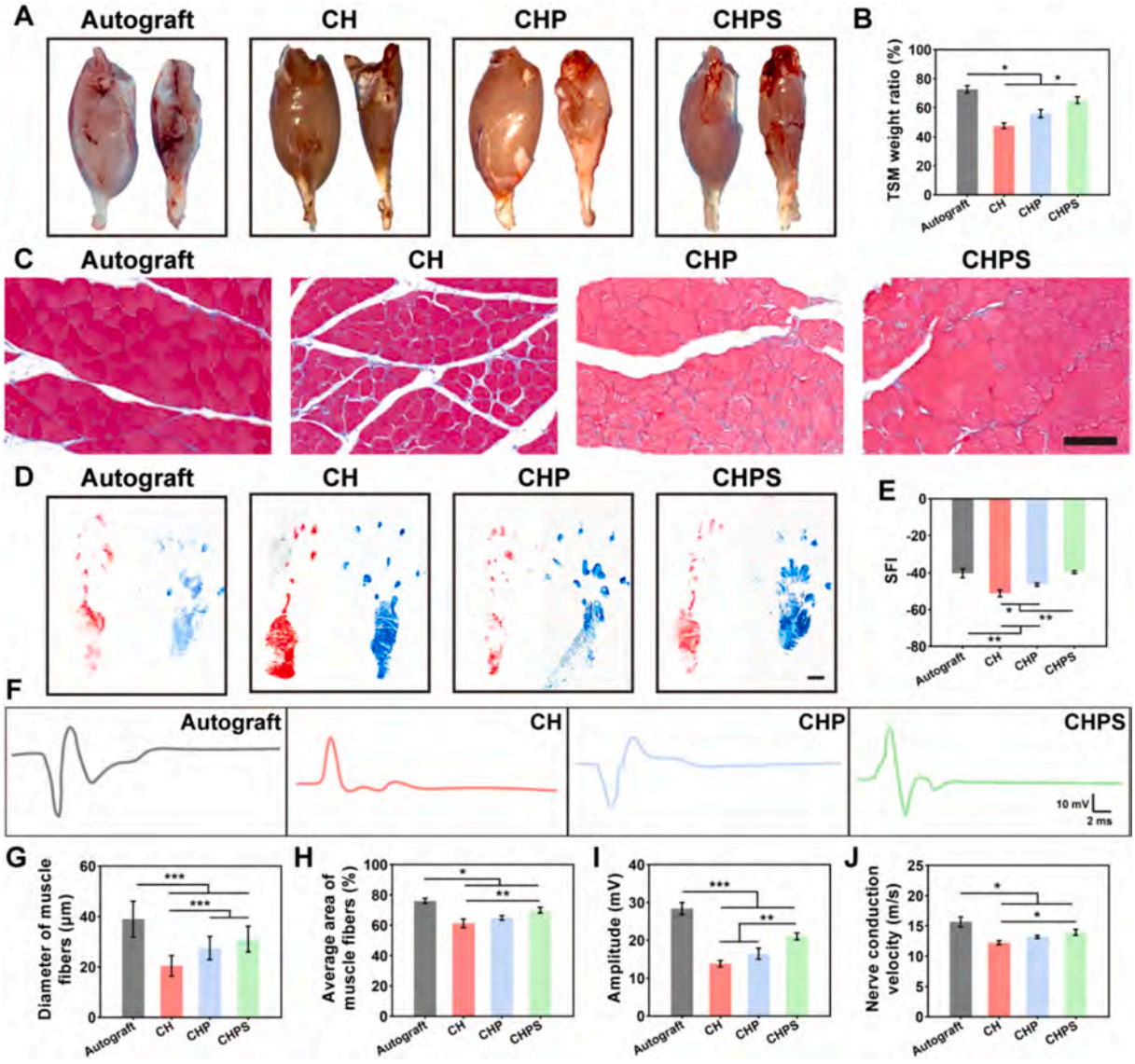

Fig. 7. Functional evaluation of nerve recovery at 12 weeks post-implantation. (A) Photographs of gastrocnemius muscles from both hind limbs. (B) Measurement of the TSM wet weight ratios of gastrocnemius muscles. (C) Images of cross sections of gastrocnemius muscles stained with Masson's trichrome. Scale bar: 100 μm. (D) Photographs of footprints. Scale bar: 0.5 cm. (E) SFI quantification of hind paws. (F) Representative CMAP recordings in the autograft, CH, CHP, and CHPS groups at the injury site. (G) Quantification of the diameter of gastrocnemius muscles. (H) Analysis of the average area of muscle fibers. (I) Quantification of CMAP amplitude and (J) nerve conduction velocity in the indicated groups. $^{*}p < 0.05$, $^{**}p < 0.01$, $^{***}p < 0.001$.

regeneration compared to CH scaffolds. Studies have shown that electrical signals in organisms play a significant role in regulating neural function and development, promoting cellular interactions, and affecting the differentiation and migration of neurons (Spitzer, 2006). The CHP and CHPS hydrogels serve as conductive scaffolds that bridge the severed nerve ends, enhancing the expression of relevant proteins and facilitating peripheral nerve repair.

3.1.4. *Anti-inflammatory properties of conduits*

To gain further insight into the inflammatory response during nerve regeneration, immunofluorescence staining was performed for iNOS (a marker of M1 macrophages) and CD206 (a marker of M2 macrophages). As shown in Fig. 6A, iNOS expression was significantly higher in the CH and CHP groups compared to the CHPS and autograft groups. In contrast, CD206 expression was significantly elevated in the CHPS group relative to the other groups. Quantitative analysis of iNOS and CD206 positive areas confirmed these observations, indicating that the CHPS conduit promoted M2 macrophage infiltration and created an anti-inflammatory microenvironment conducive to nerve regeneration (Fig. 6B and C). Statistical analysis revealed that the M2/M1 ratio in the CHPS group was significantly higher than that in the CH and CHP groups (Fig. 6D). This finding indicated that the CHPS conduit exhibited anti-inflammatory properties, alleviated the inflammatory response, and contributed to the formation of the anti-inflammatory microenvironment for nerve regeneration. Although several studies have reported that SIM inhibits M1 macrophage polarization, the specific mechanisms remain to be thoroughly investigated. This may partially explain why M2-type macrophages in the CHPS conduits maintain higher numbers in the later stages of peripheral nerve repair (Zhao et al., 2022).

3.1.5. *Functional evaluation of regenerated sciatic nerves*

The efficacy of sciatic nerve repair in the experimental groups was assessed based on the recovery of motor function and nerve conduction function after surgery (Hu et al., 2024). The gastrocnemius muscle is the target organ of the sciatic nerve, and the extent of its atrophy may indicate the extent of neuromotor recovery. At 12 weeks post-operation,

gastrocnemius muscles were harvested for quantitative analysis. Specifically, the left side represented the uninjured control, while the right side corresponded to the surgical condition (Fig. 7A). Statistical results revealed that the TSM weight ratio of the CHPS NGCs was the closest to that of the autograft group and was significantly higher compared to the CH and CHP groups. These findings suggested that the CHPS group exhibited less muscle atrophy than the CH and CHP groups (Fig. 7B). Masson's trichrome staining of muscle sections was performed to further analysis of muscle atrophy (Fig. 7C). Statistical analysis of muscle fiber diameter and average muscle area illustrated that the CHPS group was closest to the autograft, and the CHP was better than the CH group (Fig. 7G and H). Recovery of motor function in rats was also assessed by footprint analysis (Fig. 7D). SFI statistics showed that there was no significant difference between the CHPS group and the autograft (Fig. 7E). In addition, the conduction of nerve action potentials is an essential indicator in evaluating peripheral nerve function (Fig. 7F). Electrophysiological results showed that action potential amplitude and nerve conduction velocity were significantly better in the CHPS group than in the CH and CHP groups (Fig. 7I and J). Collectively, these results suggested a potential advantage of CHP and CHPS NGCs over CH NGCs in promoting nerve conduction function. It should be noted that the electrophysiological recordings were conducted using conventional stimulation methods. Further research employing more refined and standardized stimulation protocols is essential to validate differences in nerve conduction function.

4. Conclusion

In conclusion, a conductive and anti-inflammatory hydrogel was constructed and injected into nerve conduits, showing potential in modulating the local inflammatory response and supporting nerve regeneration. The in situ polymerization of PEDOT within the CHP and CHPS hydrogels exhibited improved and stable electrical conductivity, effectively promoting the proliferation of SCs and PC12 cells under ES. Upon activation of SIM, the anti-inflammatory drug was uniformly dispersed within the CHPS hydrogel, facilitating its sustained release at the injury site to create an anti-inflammatory microenvironment that prevented inflammation-induced inhibition of peripheral nerve regeneration. The CHPS hydrogel-filled nerve conduit may serve as a promising candidate for peripheral nerve repair, although further mechanistic studies are needed to confirm its exact mode of action.

CRediT authorship contribution statement

Jiahui Song: Methodology, Conceptualization, Writing – original draft. **Chenlong Liao:** Methodology, Data curation. **Zhengchao Yuan:** Project administration, Investigation, Formal analysis. **Xiao Yu:** Supervision, Methodology. **Jie Cui:** Validation, Software. **Yangfan Ding:** Resources, Investigation. **Panpan Shang:** Software, Resources. **Jinglei Wu:** Resources, Investigation. **Binbin Sun:** Validation, Supervision. **Mohamed EL-Newehy:** Visualization, Funding acquisition. **Meera Moydeen Abdulhameed:** Visualization, Funding acquisition. **Wenchuan Zhang:** Supervision, Project administration. **Gen Wen:** Validation, Investigation. **Shichao Jiang:** Resources, Methodology. **Xiumei Mo:** Investigation, Writing – review & editing.

Declaration of competing interest

The authors declare that they have no known competing financial interests or personal relationships that could have appeared to influence the work reported in this paper.

Acknowledgements

This work was supported by the Fundamental Research Funds for the Central Universities (24D311703), Science and Technology Commission of Shanghai Municipality, China (20DZ2254900), Sino German Science Foundation Research Exchange Center, China (M-0263), China Education Association for International Exchange (2022181), National Key Research and Development Program of China (2021FYC2400800), National Natural Science Foundation of China (81801219, 82271389), Natural Science Foundation of Shanghai (21ZR1438100), Medical Innovation Research Project of the Shanghai Science and Technology Commission (21Y11906300), and the Chenguang Program of Shanghai Education Development Foundation and Shanghai Municipal Education Commission (23CGB08). This project was also supported by Ongoing Research Funding program (ORF-2025-65), King Saud University, Riyadh, Saudi Arabia.

Appendix A. Supplementary data

Supplementary data to this article can be found online at https://doi.org/10.1016/j.carbpol.2025.124178.

Data availability

All data that support the findings of this study are included in the paper and the Supporting information. Additional data related to this paper are available from the corresponding author upon reasonable request.

References

Abe, G. L., Sasaki, J.-I., Katata, C., Kohno, T., Tsuboi, R., Kitagawa, H., & Imazato, S. (2020). Fabrication of novel poly(lactic acid/caprolactone) bilayer membrane for GBR application. *Dental Materials, 36*, 626–634.

Bashir, S. M., Ahmed Rather, G., Patrício, A., Haq, Z., Sheikh, A. A., Shah, M. Z. U. H., … Fonte, P. (2022). Chitosan nanoparticles: A versatile platform for biomedical applications. *Materials, 15*, 6521.

Chalfoun, C., Scholz, T., Cole, M. D., Steward, E., Vanderkam, V., & Evans, G. R. D. (2003). Primary nerve grafting: A study of revascularization. *Microsurgery, 23*, 60–65.

Deng, P., Chen, F., Zhang, H., Chen, Y., & Zhou, J. (2022). Multifunctional double-layer composite hydrogel conduit based on chitosan for peripheral nerve repairing. *Advanced Healthcare Materials, 11*, Article 2200115.

Escobar, A., Serafin, A., Carvalho, M. R., Culebras, M., Cantarero, A., Beaucamp, A., … Collins, M. N. (2023). Electroconductive poly(3,4-ethylenedioxythiophene) (PEDOT) nanoparticle-loaded silk fibroin biocomposite conduits for peripheral nerve regeneration. *Advanced Composites and Hybrid Materials, 6*, Article 42114.

Fan, L., Liu, C., Chen, X., Zheng, L., Zou, Y., Wen, H., … L. Ning, C. Y. (2022). Exosomes-loaded electroconductive hydrogel synergistically promotes tissue repair after spinal cord injury via immunoregulation and enhancement of myelinated axon growth. *Advanced Science, 9*, Article 2105586.

Fan, N. S., Da Ding, H., Yang, H., Xu, C., Wang, C., & Yang, Y. (2025). E-jet 3D printed aligned nerve guidance conduits incorporated with decellularized extracellular matrix hydrogel encapsulating extracellular vesicles for peripheral nerve repair. *Acta Biomaterialia, 194*, 122–139.

Gong, B., Zhang, X., Zahrani, A. A., Gao, W., Ma, G., Zhang, L., & Xue, J. (2022). Neural tissue engineering: From bioactive scaffolds and in situ monitoring to regeneration. *Exploration, 2*, Article 20210035.

Gu, X.-S., He, F., Chu, X.-L., Song, X.-Z., Li, Q., Li, Y.-R., & Ming, D. (2022). Basic mechanisms of peripheral nerve injury and treatment via electrical stimulation. *Neural Regeneration Research, 17*, 2185–2193.

Guan, S., Wang, Y., Xie, F., Wang, S., Xu, W., Xu, J., & Sun, C. (2022). Carboxymethyl chitosan and gelatin hydrogel scaffolds incorporated with conductive PEDOT nanoparticles for improved neural stem cell proliferation and neuronal differentiation. *Molecules, 27*, 8326.

Guo, Q., Liu, C., Hai, B., Ma, T., Zhang, W., Tan, J., Fu, X., Wang, H., Xu, Y., & Song, C. (2017). Chitosan conduits filled with simvastatin/Pluronic F-127 hydrogel promote peripheral nerve regeneration in rats. *Journal of Biomedical Materials Research Part B: Applied Biomaterials, 106*, 787–799.

Han, Y., Sun, M., Lu, X., Xu, K., Yu, M., Yang, H., & Yin, J. (2024). A 3D printable gelatin methacryloyl/chitosan hydrogel assembled with conductive PEDOT for neural tissue engineering. *Composites Part B: Engineering, 273*, Article 111241.

Hoemann, C. D., Chenite, A., Sun, J., Hurtig, M., Serreqi, A., Lu, Z., Rossomacha, E., & Buschmann, M. D. (2007). Cytocompatible gel formation of chitosan-glycerol phosphate solutions supplemented with hydroxyl ethyl cellulose is due to the presence of glyoxal. *Journal of Biomedical Materials Research Part A, 83a*, 521–529.

Hu, C., Liu, B., Huang, X., Wang, Z., Qin, K., Sun, L., & Fan, Z. (2024). Sea cucumber-inspired microneedle nerve guidance conduit for synergistically inhibiting muscle atrophy and promoting nerve regeneration. *ACS Nano, 18*, 14427–14440.

Jafari, M., Hojati, V., Khaksari, M., & Vaezi, G. (2021). Simvastatin attenuates spatial memory impairment via inhibiting microgliosis and apoptotic cell death against

ethanol induced neurotoxicity in the developing rat hippocampus. *Brain Research, 1758*, Article 147341.
Jin, S., Jung, H., Song, J., Kim, S., Yoon, S., Kim, J. H., … Shin, M. (2025). Adhesive and conductive fibrous hydrogel bandages for effective peripheral nerve regeneration. *Advanced Healthcare Materials, 14*, Article 2403722.
Lee, J. H., Yoon, Y. C., Kim, H. S., Lee, J., Kim, E., Findeklee, C., & Katscher, U. (2022). In vivo electrical conductivity measurement of muscle, cartilage, and peripheral nerve around knee joint using MR-electrical properties tomography. *Scientific Reports, 12*, Article 41598.
Li, L., Chu, Z., Li, S., Zheng, T., Wei, S., Zhao, Y., … Lu, Q. (2024). BDNF-loaded chitosan-based mimetic mussel polymer conduits for repair of peripheral nerve injury. *Frontiers in Cell and Developmental Biology, 12*, Article 1431558.
Liang, F., Yang, Y., Chen, Y., Xie, J., Liu, S., Tan, Z., … Yang, Q. (2023). Ropivacaine microsphere-loaded electroconductive nerve dressings for long-acting analgesia and functional recovery following diabetic peripheral nerve injury. *Materials Today Bio, 21*, Article 100712.
Liu, C., Fan, L., Tian, Z., Wen, H., Zhou, L., Guan, P., … Liu, B. (2021). Self-curling electroconductive nerve dressing for enhancing peripheral nerve regeneration in diabetic rats. *Bioactive Materials, 6*, 3892–3903.
Liu, X. Y., & Duan, X. C. (2023). Mechanisms and treatments of peripheral nerve injury. *Annals of Plastic Surgery, 91*, 313–318.
Madivoli, E. S., Schwarte, J. V., Kareru, P. G., Gachanja, A. N., & Fromm, K. M. (2023). Stimuli-responsive and antibacterial cellulose-chitosan hydrogels containing polydiacetylene nanosheets. *Polymers, 15*.
Mahar, M., & Cavalli, V. (2018). Intrinsic mechanisms of neuronal axon regeneration. *Nature Reviews Neuroscience, 19*, 323–337.
Montaner, J., Cano-Sarabia, M., Simats, A., Hernández-Guillamon, M., Rosell, A., Maspoch, D., & Campos-Martorell, M. (2016). Charge effect of a liposomal delivery system encapsulating simvastatin to treat experimental ischemic stroke in rats. *International Journal of Nanomedicine, 11*, 3035–3048.
Osborne, N. R., Anastakis, D. J., & Davis, K. D. (2018). Peripheral nerve injuries, pain, and neuroplasticity. *Journal of Hand Therapy, 31*, 184–194.
Park, T., Jeong, J., Kim, Y. J., & Yoo, H. (2022). Weak molecular interactions in organic composite dry film lead to degradable, robust wireless electrophysiological signal sensing. *Advanced Materials Interfaces, 9*, Article 2200594.
Saffari, T. M., Bedar, M., Hundepool, C. A., Bishop, A. T., & Shin, A. Y. (2020). The role of vascularization in nerve regeneration of nerve graft. *Neural Regeneration Research, 15*, 1573–1579.
Shan, Y., Xu, L., Cui, X., Wang, E., Jiang, F., Li, J., … Li, Z. (2024). A responsive cascade drug delivery scaffold adapted to the therapeutic time window for peripheral nerve injury repair. *Materials Horizons, 11*, 1032–1045.
Sharma, S., Kirwale, S. S., Katakia, Y. T., Majumder, S., & Roy, A. (2023). Development and evaluation of a simvastatin-loaded biopolymeric scaffold for improved angiogenesis and healing of diabetic wounds. *Journal of Drug Delivery Science and Technology, 87*, Article 104832.
Singh, V. K., Haq, A., Tiwari, M., & Saxena, A. K. (2022). Approach to management of nerve gaps in peripheral nerve injuries. *Injury-International Journal of the Care of the Injured, 53*, 1308–1318.
Spencer, A. R., Primbetova, A., Koppes, A. N., Koppes, R. A., Fenniri, H., & Annabi, N. (2018). Electroconductive gelatin methacryloyl-PEDOT:PSS composite hydrogels: Design, synthesis, and properties. *ACS Biomaterials Science & Engineering, 4*, 1558–1567.
Spitzer, N. C. (2006). Electrical activity in early neuronal development. *Nature, 444*, 707–712.
Stüve, O., Youssef, S., Steinman, L., & Zamvil, S. S. (2003). Statins as potential therapeutic agents in neuroinflammatory disorders. *Current Opinion in Neurology, 16*, 393–401.
Wang, J. W., Guo, Z. H., Xiong, J. X., Wu, D. T., Li, S., Tao, Y. X., … Kong, Y. (2019). Facile synthesis of chitosan-grafted beta-cyclodextrin for stimuli-responsive drug delivery. *International Journal of Biological Macromolecules, 125*, 941–947.
Wang, R., Shou, D., Lv, O., Kong, Y., Deng, L. H., & Shen, J. (2017). pH-controlled drug delivery with hybrid aerogel of chitosan, carboxymethyl cellulose and graphene oxide as the carrier. *International Journal of Biological Macromolecules, 103*, 248–253.
Wang, X., Chen, S., Chen, X., Wu, J., Huang, Z., Wang, J., … Liu, C. (2024). Biomimetic multi-channel nerve conduits with micro/nanostructures for rapid nerve repair. *Bioactive Materials, 41*, 577–596.
Wu, S., Shen, W., Ge, X., Ao, F., Zheng, Y., Wang, Y., … Luo, Y. (2023). Advances in large gap peripheral nerve injury repair and regeneration with bridging nerve guidance conduits. *Macromolecular Bioscience, 23*, Article 2300078.
Xu, C., Wu, P., Yang, K., Mu, C., Li, B., Li, X., … Luo, Z. (2023). Multifunctional biodegradable conductive hydrogel regulating microenvironment for stem cell therapy enhances the nerve tissue repair. *Small, 20*, Article 2309793.
Yan, S., Ren, J., Jian, Y., Wang, W., Yun, W., & Yin, J. (2018). Injectable maltodextrin-based micelle/hydrogel composites for simvastatin-controlled release. *Biomacromolecules, 19*, 4554–4564.
Yan, S., Yin, J., Tang, L., & Chen, X. (2010). Novel physically crosslinked hydrogels of carboxymethyl chitosan and cellulose ethers: Structure and controlled drug release behavior. *Journal of Applied Polymer Science, 119*, 2350–2358.
Ye, B. T. L., Zhou, G. D., Li, J. J., Ma, Y., Zhang, Y. X., Chen, Y., & J. H.. (2024). Sulfated glyco-based hydrogels as self-healing, adhesive, and anti-inflammatory dressings for wound healing. *Colloids and Surfaces, B: Biointerfaces, 238*, Article 113915.
Yu, J., Huang, X., Chen, X., Hu, P., Liu, T., Zhang, T., Cheng, R., Cui, T., & Li, J. (2024). Antibacterial and anti-inflammatory Bi-functional carbon dots hydrogel dressing for robust promotion of wound healing. *Carbon, 226*, Article 119209.
Yu, M., Liu, W., Li, J., Lu, J., Lu, H., Jia, W., & Liu, F. (2020). Exosomes derived from atorvastatin-pretreated MSC accelerate diabetic wound repair by enhancing angiogenesis via AKT/eNOS pathway. *Stem Cell Research & Therapy, 11*, Article 13287.
Yu, T., Zhao, C. F., Li, P., Liu, G. Y., & Luo, M. (2013). Poly(lactic-co-glycolic acid) conduit for repair of injured sciatic nerve. *Neural Regeneration Research, 8*, 1966–1973.
Yu, X., Shen, Y., Cui, J., Ding, Y., Morsi, Y., Sun, B., … Gu, H. (2025). The potential application of electrical stimulation in tendon repair: A review. *Med-X, 3*, Article 44258.
Zhang, S., Wang, J., Zheng, Z., Yan, J., Zhang, L., Li, Y., Zhang, J., Li, G., Wang, X., & Kaplan, D. (2021). Porous nerve guidance conduits reinforced with braided composite structures of silk/magnesium filaments for peripheral nerve repair. *Acta Biomaterialia, 134*, 116–130.
Zhang, X., Ma, Y., Chen, Z., Jiang, H., & Fan, Z. (2023). Implantable nerve conduit made of a self-powered microneedle patch for sciatic nerve repair. *Advanced Healthcare Materials, 12*, Article 2301729.
Zhao, R., Ning, X., Wang, M., Wang, H., Xing, G., Wang, L., … Wang, Y. (2022). A ROS-responsive simvastatin nano-prodrug and its fibronectin-targeted co-delivery system for atherosclerosis treatment. *ACS Applied Materials & Interfaces, 14*, 25080–25092.
Zhou, B., Song, J. Z., Wang, B., Feng, Y. Z., Liu, C. T., & Shen, C. Y. (2022). Robust double-layered ANF/MXene-PEDOT:PSS Janus films with excellent multi-source driven heating and electromagnetic interference shielding properties. *Nano Research, 15*, 9520–9530.
Zhou, L., Fan, L., Yi, X., Zhou, Z., Liu, C., Fu, R., … Ning, C. (2018). Soft conducting polymer hydrogels cross-linked and doped by tannic acid for spinal cord injury repair. *ACS Nano, 12*, 10957–10967.
Zuo, K. J., & Borschel, G. H. (2021). A retrospective case series reporting the outcomes of Avance nerve allografts in the treatment of peripheral nerve injuries. *Plastic and Reconstructive Surgery, 147*, 368–381.